GIANT LOW SURFACE BRIGHTNESS GALAXIES AS MERGER REMNANTS

Peter Yoachim[1], Denise Schmitz[4], Sarah Loebman[2], SungWon Kwak[5,6], Victor P. Debattista[3]
Draft version May 4, 2018

ABSTRACT

We present IFU observations of the giant low surface brightness galaxies Malin 2 and UGC 6614. We fit the stellar dynamics of these systems and compare their spatially resolved spectra to star formation history models. We argue that Malin 2 and UGC 6614 are normal elliptical galaxies that have undergone high angular momentum mergers which formed their GLSB disks, making them unique systems for probing the dark matter halos of elliptical systems. We find the stellar dynamics are consistent with earlier measurements of the GLSB H I disks. The stellar populations of the GLSB disks are dominated by old metal-poor stars, while the central ellipticals are metal rich.

Subject headings: galaxies: kinematics and dynamics — galaxies: formation — galaxies: structure

1. INTRODUCTION

Since the discovery of Malin 1 (Bothun et al. 1987), giant low surface brightness galaxies (GLSB) have presented a unique problem for galaxy formation theories. Low surface brightness (LSB) galaxies are typically defined as disks with central surface brightnesses fainter than 23 B mag arcsec^2. While LSB galaxies span a wide range of sizes and masses, the few giant low surface brightness that have been discovered seem to be unrelated objects that are at least an order of magnitude larger in extent than typical LSB systems.

Observers tend to classify GLSB systems as normal spirals. Matthews et al. (2001) list Malin 2 as an Scd while Das (2013) conclude that GLSB systems are an extreme form of late type spiral galaxies. Similarly, Kasparova et al. (2014) claim that the large dark matter scale of Malin 2 can explain it's features. Even the Galaxy Zoo project (Willett et al. 2013) classifies GLSB galaxies as spirals. While GLSB systems superficially resemble normal spiral galaxies, they are clearly extreme outliers when their scale lengths are compared to other galaxy samples, being around a factor of 2 larger than the largest normal spirals (Dalcanton et al. 1997, Figure 4).

The disks in GLSB systems are incredibly large, with Malin 1 being detected in R-band to a radius of over 100 kpc (Moore & Parker 2006). Disks of this size are a challenge for typical ΛCDM cosmology galaxy formation theories and more exotic formation scenarios have been proposed for GLSB systems. Mapelli et al. (2008) form GLSB-like galaxies in simulations via the fading of collisional ring galaxies. In their model, a collision sets off an expanding ring of star formation. As the star formation subsides and the stellar population ages, the ring galaxy fades over ∼100 Myr to resembles observed GLSBs. One

obvious problem with this scenario is that most GLSB's are relatively isolated, and thus there are no obvious candidates for the impactor systems that would have triggered the star formation burst.

The other popular formation scenario for GLSB systems is that they are normal galaxies that undergo a high angular momentum minor merger where the LSB disk is the shredded remains of an accreted galaxy. Peñarrubia et al. (2006) find that extended disks can be formed via the disruption of dwarf galaxies. These simulated debris disks have exponential profiles and extend out to 200 kpc from the central galaxy.

Observations of Malin 1 support the accretion model of GLSBs. Barth (2007) analyzes HST imaging of Malin 1 and find that the central object is well described as a normal early-type barred galaxy that was previously unresolved in ground-based imaging. Barth (2007) points out that extended disk structures in galaxies such as M31 appear to be a smooth continuation of the inner disk (Ferguson et al. 2002), while Malin 1's extended disk is better described as a distinct component, (although Ibata et al. (2005) claim M31's extended disk is of accretion origin).

If GLSB disks are indeed the remains of accreted dwarf galaxies, they represent a unique opportunity to observationally probe the outer regions of galaxy dark matter halos, especially if they form around elliptical galaxies. The mass profiles of elliptical galaxies have been difficult to constrain since they lack the extended H I disks found around spirals. As an example of how difficult it can be to measure the outer regions of elliptical galaxy kinematics, Murphy et al. (2011) model M87 out to ∼23 kpc with stellar kinematics and out to 51 kpc with globular clusters (or $R = 4.8R_e$, where R_e is the effective radius). Raskutti et al. (2014) are also limited to measuring kinematics out to ∼2-5 R_e.

In comparison, the stellar disk of Malin 2 extends beyond 40 kpc (5.9 R_e), and the HI disk reaches beyond 100 kpc (14.8 R_e). Galaz et al. (2015) take deep images of Malin 1 and find the stellar disk diameter extends to 160 kpc.

In one of the most extensive studies of a GLSB system, Kasparova et al. (2014) combine ARC 3.5m photometry and long-slit spectra with Gemini spectra to mass-model Malin 2. They find the broadband colors of the extended

[1] Department of Astronomy, University of Washington, Box 351580, Seattle WA, 98195
[2] University of Michigan
[3] Jeremiah Horrocks Institute, University of Central Lancashire, Preston PR1 2HE, UK.
[4] California Institute of Technology
[5] Center for the Exploration of the Origin of the Universe (CEOU), Department of Physics & Astronomy, Seoul National University, Seoul 151-742, Republic of Korea
[6] Korea Astronomy and Space Science Institute, Daejeon 305-348, Republic of Korea

disk are not consistent with a catastrophic formation, but are best fit by an exponentially declining SFH. They speculate the main difference between Malin 2 and non-giant LSB galaxies is the dark matter halo scale. To some extent, this is not a particularly satisfying conclusion because one is then left with the mystery of why Malin 2's dark matter halo is so different from non-giant galaxies.

In §2 we present new observations of Malin 2 and UGC 6614. In §3, we compare the general properties of GLSB galaxies to samples of galaxies drawn from the Sloan Digital Sky Survey (SDSS) and The H INearby Galaxy Survey (THINGS). In §4 and §5 we measure the stellar kinematics and star formation histories from our spectra. In §6, we discuss what our observations imply for the possible formation mechanisms for GLSB systems.

2. OBSERVATIONS

We obtained spatially resolved spectroscopy of our target galaxies using the Mitchell Spectrograph (formerly VIRUS-P)(Hill et al. 2008) on the 2.7m Harlan J. Smith telescope at McDonald Observatory. Observations were made during dark time in February, March, and April 2010. Identical instrument setups were used for all observations. The Mitchell Spectrograph with the VP-2 IFU bundle used here has a square array of 246 optical fibers which sample the $1.9' \times 1.9'$ field-of-view with a 1/3 filling factor, with each fiber having a diameter of $4.23''$. The spectrograph images the spectrum of each fiber on a 2048×2048 Fairchild Imaging CCD.

For each galaxy, observations were taken at three unique dither positions to provide nearly complete spatial coverage. Individual science exposures were 30 minutes. Malin 2 had 10 exposures per dither position (11 exposures for dither position 1), for a total of 15 hours of exposure time. Observations of UGC 06614 had alignment issues between observing runs. This resulted in a deep stack of 6 exposures, and a shallow stack with only 2 exposures. With only 2 exposures, cosmic ray rejection becomes unreliable, therefore, we use these shallow frames when looking at the surface brightness profiles, but use only the aligned deep co-add when analyzing the stellar kinematics and stellar populations. Twilight flat field frames, bias frames, and wavelength calibration Hg and Cd lamps were taken during the day. Flux standard stars were observed in twilight.

We use the Mitchell Spectrograph software pipeline Vaccine (Adams et al. 2011) to perform basic reduction tasks. Vaccine subtracts the over-scan region and generates and subtracts a bias frame. Bad pixels are masked. Twilight flats and arc lamps from each night are combined. The combined flat frame is used to trace the spatial profile of each fiber and correct for pixel-to-pixel variation. The combined arc lamp is used to fit a wavelength solution for each fiber. We use a 4th order polynomial and find the wavelength solutions have a typical RMS of 0.06-0.2 Å (~ 0.1 pixel). Vaccine then masks potential cosmic rays and collapses each fiber to a one dimensional spectrum. The fibers are adequately spaced, and our targets are predominately low surface brightness, so we find making a fiber cross-talk correction unnecessary.

Once the Vaccine routines are completed we make the following additional reductions using standard IRAF routines and custom IDL scripts. The reduced twilight frames are used to generate a fiber-to-fiber flux correction (similar to a longslit illumination correction). We use the b-spline procedure described in Kelson (2003) to generate background frames. The corners of the IFU array contain enough empty fibers to measure the sky background in each exposure. Because we bin fibers together, imperfect sky-subtraction represents a serious source of potential systematic errors.

The spectra are then rectified to a common wavelength scale, and the photo-spectroscopic standards are used to flux calibrate the spectra and correct for atmospheric extinction. The spectra are then velocity shifted to the Local Standard of Rest. Images taken at identical dither positions are averaged together with outlier rejection to eliminate any remaining cosmic rays. Some observations were taken in non-photometric conditions, so before combining frames we scale them to a common average flux level.

Our final reduced data for each galaxy includes 738 spectra spanning a $1.9' \times 1.9'$ field-of-view. The spectra have a wavelength range of ~ 3550-5840 with 2.2 Å pixels (with some fibers only reaching 5500 Å due to the warping of the trace). The FWHM of reduced arc lamp images is 5.3 Å, giving us a resolution of $R \sim 700 - 1000$. The fiber-to-fiber changes in resolution are less than 10%.

With our final reduced data cubes, we used Penalized Pixel-Fitting (pPXF) (Cappellari & Emsellem 2004) and Gas AND Absorption Line Fitting (GANDALF) (Sarzi et al. 2006) on each fiber to fit stellar velocities, stellar dispersions, and emission line velocities and fluxes. For stellar templates we use a suite of SSP spectra from Bruzual & Charlot (2003). We use GANDALF to measure the [O II] doublet, [O III] doublet, and the higher order Balmer lines Hβ, Hγ, Hδ, Hϵ while masking the night skyline at 5577 Å. The fit also includes a 4th degree multiplicative polynomial to correct for any dust or flux calibration mis-match between the observations and templates. Because our data do not extend out to Hα, we cannot use the Balmer decrement to place tight constraints on the dust extinction. While pPXF fits the stellar velocity dispersion, our instrumental resolution is low enough (~ 140 km s^{-1}) that we are unable to make meaningful velocity dispersion measurements beyond the central fibers.

In addition to individual fibers, we have binned sets of three neighboring fibers together to boost the signal-to-noise ratio and run pPXF on these super-fibers. The fiber surface brightnesses are plotted in Figures 4 and 10, and the pPXF stellar velocity maps are shown in Figures 6 and 15.

3. COMPARISONS TO OTHER GALAXIES

By eye, GLSB systems resemble large faint spiral disks at large radii, and regular ellipticals at their centers. In the Sloan Digital Sky Survey Data Release 10 (SDSS DR10) (Ahn et al. 2014), the Galaxy Zoo classifications (Willett et al. 2013) are spiral for Malin 1, Malin 2, and UGC 6614. In this section, we compare the properties of the GLSB centers and disks with other systems.

3.1. *GLSB Centers*

Both of our objects, as well as Malin 1, have been observed with SDSS, making it possible to compare them

TABLE 1
BASIC PROPERTIES OF GLSB GALAXIES

Name	SDSS ID (DR 10)	z	r (mag)	R_e arcsec	σ km s^{-1}	H I Mass $\log_{10} M_\odot$	Stellar Mass $\log_{10} M_\odot$
Malin 1	1237661068728139925	0.083	16.70	1.86	177	10.9	11.1
Malin 2	1237667735572381852	0.046	14.34	7.17	202	10.6	11.3
UGC 06614	1237668585435365393	0.021	13.52	7.3	150	10.5	10.9

NOTE. — H I masses updated to our adopted cosmological parameters from Pickering et al. (1997). The rest taken from SDSS. Stellar masses calculated from Conroy et al. (2009)

TABLE 2
FITTED STRUCTURAL PROPERTIES

Name	h_r (arcsec)	inclination (deg)
Malin 2	6.1	35.5
UGC 06614	5.7	33.4

to a large number of systems. The outer disks of GLSBs are faint enough that the SDSS photometric pipeline effectively ignores them.

To make a comparison sample of galaxies from SDSS, we select galaxies with redshifts between 0.01 and 0.07 and de-reddened r magnitude between 13.5 and 17.7. When comparing to just elliptical galaxies we make the additional color-cut of $u - r > 2.1$ (and some morphology cuts). These are simply galaxies for comparison, not a rigorously defined volume-complete sample. Our full SQL queries are shown in §A. This gives us a sample of 141,001 objects, 45,703 of which have red colors. Throughout, we use the CosmoloPy[7] fiducial cosmology ($h = 0.704$, $\Omega_{m_0} = 0.2726$, $\Omega_{\lambda_0} = 0.7274$). Note that we are not correcting for Malmquist bias or biases in the SDSS spectroscopic selection criteria. Our selection is simply for galaxies of a similar magnitude and redshift.

Figure 1 shows where the GLSBs fall on the major galaxy relations. We use extinction corrected magnitudes and k-corrected colors (Chilingarian et al. 2010). Both of our GLSBs lie on the red-sequence in the color-magnitude diagram.

The central regions of GLSBs are often referred to in the literature as "bulges", however, looking at Figure 1, it is clear that these are much brighter than bulges of typical spiral galaxies and the centers of GLSBs are on the bright end of the red-sequence.

We follow Bernardi et al. (2003a,b) in fitting fundamental plane parameters to our selected SDSS galaxies. We fit the fundamental plane by minimizing χ^2 in,

$$\chi^2 = \log R_0 - a \log \sigma - b \log I_0 - c \qquad (1)$$

where R_0 is the galaxy's effective radius, σ is velocity dispersion in kilometers per second and I_0 is the surface brightness. The resulting best-fit parameters are $a = 1.376$, $b = -0.661$, $c = -9.938$. We note that we have not made a rigorous volume-complete selection of galaxies, rather, simply selected galaxies with similar magnitudes, colors, and redshifts to our GLSBs. See Saulder et al. (2013) for a more rigorous analysis of the fundamental plane in SDSS.

3.2. *GLSB Disks*

The diameters of GLSB disks are very large, with Malin 1's stellar disk detected out to a radius of 80 kpc (Galaz et al. 2015). Stellar disks are typically embedded in much larger H I disks. In Figure 2, we compare the sizes of the stellar and H I disks of the GLSB galaxies with other observations. For this plot, we take the maximum detected radius from the literature for the galaxies. It is possible that deeper observations could increase the values of R_{max}. While the stellar disk of UGC 6614 is close in size to local observed H I disks, Malin 1 and 2 are larger than the H I disks observed in the THINGS survey. This seems to point against the GLSB formation mechanism of Mapelli et al. (2008), as we do not observe H I disks in normal spirals large enough to convert into GLSB systems unless an interaction is able to also boost the angular momentum of the resulting stellar disk.

4. KINEMATICS

As we have shown in §3.1 and §3.2, GLSB galaxies can be well described as large normal ellipticals that have managed to accrete a high angular momentum disk of stars and gas. Given the total H I mass in GLSBs, the accreted object is consistent with a much lower-mass gas-rich spiral. If this is in fact the way GLSBs form, the disk kinematics represent a unique probe of the dark matter halo of elliptical galaxies.

We use the kinemetry package presented in Krajnović et al. (2006) to fit a tilted-ring model to the stellar kinematics. For these fits, we hold the position angle and inclination fixed to values found from fitting the fiber-photometry. Figures 6 and 15 show the kinemetry fits and extracted rotation curves. We iterate the fit, clipping residuals which deviate from the model by more than 250 km s^{-1}.

While we are making rather sweeping assumptions about the nature of the GLSB disks by fitting a simple disk with fixed position angle and inclination, the fits are quite good. We also note that by observing disks, we do not have to worry about the velocity anisotropy parameter that traditionally makes dynamical modeling of ellipticals difficult.

The Malin 2 rotation curve (Figure 6) is rather complicated, having several abrupt rises. This is especially strange given the very smooth photometric profile. UGC 6614 (Figure 15), on the other hand, has a typical late-type galaxy rotation curve with a linear rise and flat outer region. One important difference is that the linear rise extends for 10 kpc.

The lack of rotation in the central regions of the galaxies is not particularly surprising, as this is the region that is flux-dominated by the central elliptical galaxy.

The extracted rotation curves imply large dark matter halos. For Malin 2, $V_{circ} \sim 280$ km s^{-1} at $R = 42$ kpc
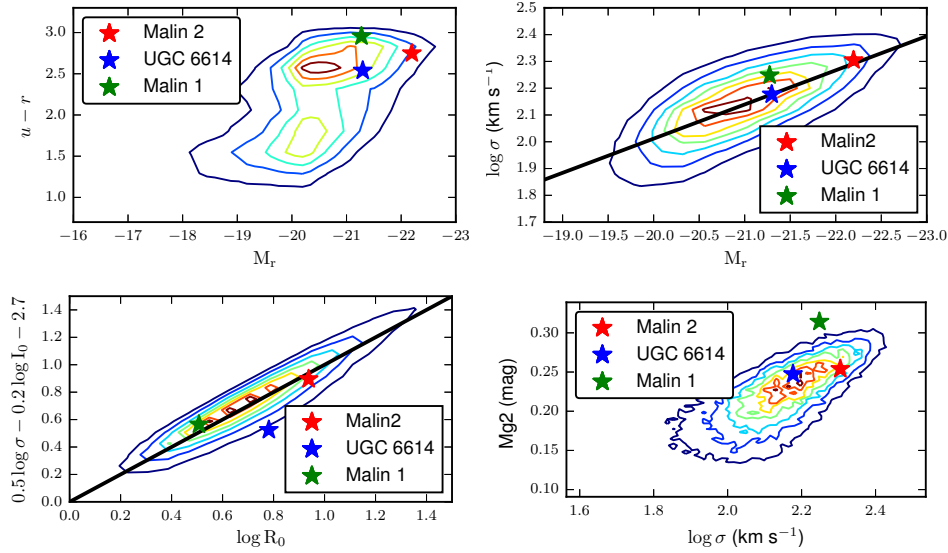
FIG. 1.— Top Left: The color-magnitude diagram for 141,000 galaxies of similar redshift and magnitude as Malin 2 and UGC 6614. Top Right: The Faber-Jackson relation for 45,700 SDSS galaxies, along with a best-fit line. Left: The r-band fundamental plane from SDSS along with our GLSB galaxies and best-fit line. Bottom Right: The relation between central velocity dispersion and the Mg2 absorption feature. From the point of view of the SDSS data reduction pipeline, GLSB galaxies appear as relatively normal red elliptical galaxies.
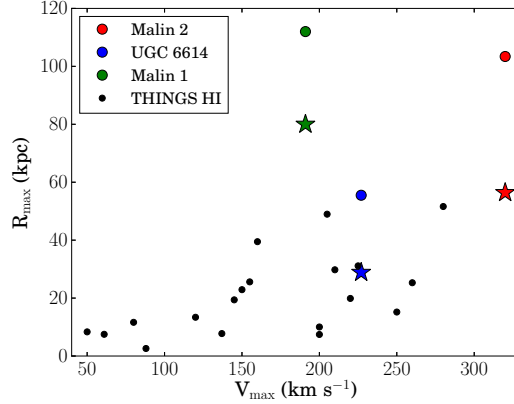
FIG. 2.— Comparison of the GLSB disks with other galaxy disks from the literature. THINGS data taken from de Blok et al. (2008), GLSB H I data from Malin 1 from Pickering et al. (1997) and GLSB stellar radii from Galaz et al. (2015), Kasparova et al. (2014), and this paper. Here, R_{max} is the maximum radius with an H I or optical detection. For the GLSB galaxies, the circular points show the maximum H I detection radius and stars-shaped points show the maximum detected stellar light radius. All points are maximum detection radii, and thus should be considered lower limits.

implies a mass of $7.6 \times 10^{11} M_\odot$ (compared to an SDSS stellar mass of 1.4×10^{11}). For UGC 6614, $V_{circ} \sim 200$ km s^{-1} at $R = 17$ kpc gives a dynamical mass of $1.6 \times 10^{11} M_\odot$ (compared to a stellar mass of $0.46 \times 10^{11} M_\odot$).

Thus, using just the stellar kinematics, for Malin 2, we reach a radius of $\sim 6.2 R_e$, and find a dark matter fraction of 81%. For UGC 6614, we reach a radius of $\sim 5.2 R_e$ and find a dark matter fraction of 71%.

Murphy et al. (2011) are able to use IFU observations of M87 to reach $\sim 2 R_e$ using just stellar data, and then rely on globular cluster kinematics to extended out to $5 R_e$ where they find a dark matter fraction of 85%. Weijmans et al. (2009) is similarly able to use IFU observations to reach $\sim 4 R_e$ on two elliptical galaxies while Proctor et al. (2009) reaches $\sim 3 R_e$ using multi-object spectroscopy.

If we use the circular speed of the H I data from the literature, we end up with dynamical masses of $25 \times 10^{11} M_\odot$

for Malin 2 and $6.5 \times 10^{11} M_\odot$ for UGC 6614 (dynamical to stellar mass ratios of 18 and 14 respectively).

5. STAR FORMATION HISTORIES

Following the work in Yoachim et al. (2010, 2012), we generate a suite of model galaxy SEDs using relatively simple star formation histories and find the single best fitting model. We break the star formation history into three age bins, 0-10 Gyr, 10-11.5 Gyr, and 11.5-12 Gyr. We assume each age bin has a constant star formation with a level of 0, 0.5, 1, or 10 solar-masses per year. Each SFH can have a metallicity of $[Z/H] = -2.3, -1.70, -0.70, -0.40, 0.0,$ or 0.40. We do not include any metallicity evolution, as all the age bins in a given model have the same metallicity. This gives us 361 unique non-zero model spectra. We use Bruzual & Charlot (2003) with a Chabrier IMF to generate the model spectra.

Figures 7 and 11 show the fibers that were binned and the resulting spectra for Malin 2 and UGC 06614. Both

galaxies have elliptical-galaxy like spectra in their centers, with outskirts that have significant emission lines. We find the best-fitting single model spectrum for each observed binned spectrum. When fitting, we include a low order multiplicative polynomial to match any dust extinction or flux calibration errors in the observations. This means our fits are for the relative star formation histories, but not the absolute star formation rates (e.g., a model constant star formation history of 1 $M_\odot$ yr^{-1} is an equally good fit as a constant 10 $M_\odot$ yr^{-1}.)

The best fitting star formation histories are shown in Figures 8 and 12, while the best fitting stellar metallicities are shown in Figures 9 and 13. We find that *both galaxies have stellar populations dominated by old stars at all radii*. While the outer disks show emission lines and are best fit with some current star formation, the total stellar mass is still overwhelmingly dominated by old stars. Both galaxies also show very steep metallicity gradients, with centers that are super-solar metallicity (at the limit of our models), while the outer disks are both best fit by [Z/H]=-0.7.

A problem with fitting observed galaxy spectra with templates is that residuals between the model and data are dominated by non-Gaussian systematic effects such as template mis-match and improper parameterization of the SFH. Since the residuals are non-Gaussian, there is no statistical formalism for generating uncertainties in the fit. To generate our error bars, we look at the range of fits which have χ^2 values within 100 of the minimum. In many cases, this eliminates nearly all fits except for the minimum. In these cases, we use the 4 best-fitting models to estimate the range of possible parameters.

The dominance of an old stellar population at large radii seems to contradict the star-burst formation mechanism of Mapelli et al. (2008), and favor an accretion model where a galaxy already containing old stars is disrupted by a massive elliptical galaxy similar to Peñarrubia et al. (2006).

6. DISCUSSION

The basic observational properties of GLSBs that need to be explained:

1. H I disks that extend much farther than typical spiral galaxies (Figure 2).

2. Total H I masses that are lower than expected given their rotational velocities (Figure 3).

3. Central bulges that are similar to massive elliptical galaxies in SDSS (Figure 1).

4. Central stellar populations that are old and very metal-rich.

5. Disk stellar populations that show signs of ongoing star formation, but are dominated by an old metal-poor population.

6. A sharp metallicity transition between the central bulge and disk components.

We find that the centers of these two GLSB systems very closely resemble normal galaxies, with the extended faint disks being distinct components, consistent with the previous results for Malin 1 (Barth 2007) and NGC 7589 (Lelli et al. 2010).

An accretion formation scenario does the best job explaining all the observations. While a collisional ring could fade to a GLSB, the stellar population should be relatively young, and one would not necessarily expect a steep metallicity gradient. Also, there are no obvious galaxies near GLSBs to act as progenitor colliders.

It also seems unlikely that GLSBs are just extreme versions of normal disk galaxies (Das 2013). It's hard to imagine how such a large massive central spheroid could be formed without also disrupting the surrounding disk. While the old stellar populations in the disks of Malin 2 and UGC 6614 are evidence against the Mapelli et al. (2008) formation scenario, we have not addressed what collisional ring galaxies do evolve into. Since photometric surveys are often surface brightness limited, it is possible a GLSB system will be found in the future that is the descendant of a collisional ring system.

One of the most important features we can see in our data is the sharp metallicity gradient as one transitions between the central region and the disk in both Malin 2 and UGC 6614 (Figures 9 and 13). For both galaxies, the best fitting star formation histories show the stellar populations are dominated by old stars inside and outside the transition, but the metallicity changes by $\sim 0.7 - 1.0$ dex. This is a very sharp gradient compared to what has been found in normal spirals for the bulge-to-disk transition region. MacArthur et al. (2009) spectroscopically observed a range of spiral galaxies and found the metallicity profiles which were dropping, rising, and flat. Using broadband colors, MacArthur et al. (2004) also found metallicity gradients were generally very shallow, with steep metallicity gradients only in very late-type spiral galaxies. Also note that our metallicity gradient could be an underestimate of the true gradient since the central metallicities are at the limits of our model grid (i.e., they could have metallicities greater than [Z/H]=0.7). We have also spatially binned data, possibly diluting how sharp the transition is between bulge and disk.

Sánchez et al. (2014) measure the Oxygen abundance from gas emission lines in a large sample of spiral galaxies and find a characteristic slope of $\alpha_{O/H} = -0.1$ dex r_e^{-1} between 0.3 and 2 effective radii. The metallicity gradients we observe in Malin 2 and UGC 6614 are factors of 2-4 steeper than the typical spiral. Also, of the 193 galaxies in Sánchez et al. (2014) only four have a slope steeper than -0.3 dex r_e^{-1} (Sánchez et al. 2014, Figure 6). In their Figure 9, they combine the data to show a typical gas metallicity curve that drops linearly until $r_e \sim 2$ and then flattens to a constant value. This shape is very different from the step function change we observe in GLSBs.

These are incredibly steep metallicity gradients. The logarithmic gradients δ[Z/H] log R/R$_e$ is ~ -1.6 for Malin 2 and ~ -0.68 for UGC 6614. These are very steep compared to gradients typically observed in elliptical galaxies (Kuntschner et al. 2010; Greene et al. 2012, 2015). Wilkinson et al. (2015) find -0.15 dex/R_e gradients for early type galaxies and flat metallicity gradients for late type galaxies.

XXX-While metallicity gradients this steep have not been observed, they do appear in simulations. Sander-
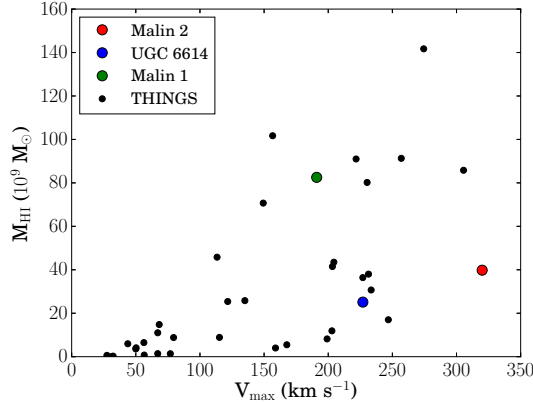
Fig. 3.— Comparison of GLSB H I masses (Pickering et al. 1997) with H I masses measured in the THINGS survey (Walter et al. 2008). While the H I masses in the GLSB systems are high, they are consistent with what would be available in a merger with a V_{max} = 100 km/s mass galaxy, and maintaining the break in stellar metallicity.

son et al. (2017) find that for their simulated Milky Way mass galaxy, there is a break in stellar metallicity that corresponds to the galactic radius where stellar populations become dominated by accretion. XXX–Should take a stab at saying how large the jump is.

Kasparova et al. (2014) present one of the most in depth observational studies of Malin 2. Mass-modeling the system, they find that a huge isothermal core with r_c = 27.3 kpc best fits the dynamics. Kasparova et al. (2014) also measure gas metallicities and find the metallicity drops from solar in the center of the system to half-solar at r = 30 kpc. It is probably foolish to directly compare gas and stellar metallicities, but it is interesting that the gas metallicity gradient appears to be much lower than the stellar gradient. This is probably consistent with a low metallicity gas-rich galaxy merging with an elliptical system that has much higher stellar metallicity, although a detailed simulation would be helpful in confirming what the final expected gas metallicity gradient should be.

Hagen et al. (2016) present the discovery of a GLSB system around UGC 1382. As in this work, they find the best explanation of the extended disk as being the remnants of an accreted dwarf galaxy similar to the simulations of Peñarrubia et al. (2006).

If these systems do prove to be ellipticals with accreted high angular momentum disks, they represent an amazing opportunity to probe the dark matter halo properties of elliptical systems to very large radii.

7. CONCLUSIONS

We have observed two giant low surface brightness galaxies with the VIRUS-P IFU. We find the systems are best explained as massive elliptical galaxies which have managed to accrete stars and gas into a large disk. We find the inner bulge is similar to elliptical galaxies found in SDSS. The extended galaxy stars have disk-like velocity fields, are dominated by old stars, but do show signs of ongoing star formation. The stars also show a sharp metallicity transition, consistent with the disk forming independently of the bulge. The H I mass of the disk is also consistent with coming from a low-mass accreted galaxy.

We are currently observing higher spatial resolution, but now publicly available Hα imaging with HST (GO 14189) and new IFU data with Gemini (GN-2015A-Q-75) of the central region of these galaxies to confirm they are normal elliptical galaxies and constrain a more sophisticated dynamical model of the system.

REFERENCES

Adams, J. J., Blanc, G. A., Hill, G. J., Gebhardt, K., Drory, N., Hao, L., Bender, R., Byun, J., Ciardullo, R., Cornell, M. E., Finkelstein, S. L., Fry, A., Gawiser, E., Gronwall, C., Hopp, U., Jeong, D., Kelz, A., Kelzenberg, R., Komatsu, E., MacQueen, P. J., Murphy, J., Odoms, P. S., Roth, M., Schneider, D. P., Tufts, J. R., & Wilkinson, C. P. 2011, ApJS, 192, 5

Ahn, C. P., Alexandroff, R., Allende Prieto, C., Anders, F., Anderson, S. F., Anderton, T., Andrews, B. H., Aubourg, É., Bailey, S., Bastien, F. A., & et al. 2014, ApJS, 211, 17

Barth, A. J. 2007, AJ, 133, 1085

Bernardi, M., Sheth, R. K., Annis, J., Burles, S., Eisenstein, D. J., Finkbeiner, D. P., Hogg, D. W., Lupton, R. H., Schlegel, D. J., SubbaRao, M., Bahcall, N. A., Blakeslee, J. P., Brinkmann, J., Castander, F. J., Connolly, A. J., Csabai, I., Doi, M., Fukugita, M., Frieman, J., Heckman, T., Hennessy, G. S., Ivezić, Ž., Knapp, G. R., Lamb, D. Q., McKay, T., Munn, J. A., Nichol, R., Okamura, S., Schneider, D. P., Thakar, A. R., & York, D. G. 2003a, AJ, 125, 1817

—. 2003b, AJ, 125, 1866

Bothun, G. D., Impey, C. D., Malin, D. F., & Mould, J. R. 1987, AJ, 94, 23

Bruzual, G., & Charlot, S. 2003, MNRAS, 344, 1000

Cappellari, M., & Emsellem, E. 2004, PASP, 116, 138

Chilingarian, I. V., Melchior, A.-L., & Zolotukhin, I. Y. 2010, MNRAS, 405, 1409

Conroy, C., White, M., & Gunn, J. E. 2009, ArXiv e-prints

Dalcanton, J. J., Spergel, D. N., & Summers, F. J. 1997, ApJ, 482, 659

Das, M. 2013, Journal of Astrophysics and Astronomy, 34, 19

de Blok, W. J. G., Walter, F., Brinks, E., Trachternach, C., Oh, S.-H., & Kennicutt, Jr., R. C. 2008, AJ, 136, 2648

Ferguson, A. M. N., Irwin, M. J., Ibata, R. A., Lewis, G. F., & Tanvir, N. R. 2002, AJ, 124, 1452

Galaz, G., Milovic, C., Suc, V., Busta, L., Lizana, G., Infante, L., & Royo, S. 2015, ApJ, 815, L29

Greene, J. E., Janish, R., Ma, C.-P., McConnell, N. J., Blakeslee, J. P., Thomas, J., & Murphy, J. D. 2015, ArXiv e-prints

Greene, J. E., Murphy, J. D., Comerford, J. M., Gebhardt, K., & Adams, J. J. 2012, ApJ, 750, 32

Hagen, L. M. Z., Seibert, M., Hagen, A., Nyland, K., Neill, J. D., Treyer, M., Young, L. M., Rich, J. A., & Madore, B. F. 2016, ArXiv e-prints

Hill, G. J., MacQueen, P. J., Smith, M. P., Tufts, J. R., Roth, M. M., Kelz, A., Adams, J. J., Drory, N., Grupp, F., Barnes, S. I., Blanc, G. A., Murphy, J. D., Altmann, W., Wesley, G. L., Segura, P. R., Good, J. M., Booth, J. A., Bauer, S., Popow, E., Goertz, J. A., Edmonston, R. D., & Wilkinson, C. P. 2008, SPIE, 7014

Ibata, R., Chapman, S., Ferguson, A. M. N., Lewis, G., Irwin, M., & Tanvir, N. 2005, ApJ, 634, 287

Kasparova, A. V., Saburova, A. S., Katkov, I. Y., Chilingarian, I. V., & Bizyaev, D. V. 2014, MNRAS, 437, 3072

Kelson, D. D. 2003, PASP, 115, 688

Krajnović, D., Cappellari, M., de Zeeuw, P. T., & Copin, Y. 2006, MNRAS, 366, 787

Kuntschner, H., Emsellem, E., Bacon, R., Cappellari, M., Davies, R. L., de Zeeuw, P. T., Falcón-Barroso, J., Krajnović, D., McDermid, R. M., Peletier, R. F., Sarzi, M., Shapiro, K. L., van den Bosch, R. C. E., & van de Ven, G. 2010, MNRAS, 408, 97

Lelli, F., Fraternali, F., & Sancisi, R. 2010, A&A, 516, A11+

MacArthur, L. A., Courteau, S., Bell, E., & Holtzman, J. A. 2004, ApJS, 152, 175

MacArthur, L. A., González, J. J., & Courteau, S. 2009, MNRAS, 395, 28

Mapelli, M., Moore, B., Ripamonti, E., Mayer, L., Colpi, M., & Giordano, L. 2008, MNRAS, 383, 1223

Matthews, L. D., van Driel, W., & Monnier-Ragaigne, D. 2001, A&A, 365, 1

Moore, L., & Parker, Q. A. 2006, Publications of the Astronomical Society of Australia, 23, 165

Murphy, J. D., Gebhardt, K., & Adams, J. J. 2011, ApJ, 729, 129

Peñarrubia, J., McConnachie, A., & Babul, A. 2006, ApJ, 650, L33

Pickering, T. E., Impey, C. D., van Gorkom, J. H., & Bothun, G. D. 1997, AJ, 114, 1858

Proctor, R. N., Forbes, D. A., Romanowsky, A. J., Brodie, J. P., Strader, J., Spolaor, M., Mendel, J. T., & Spitler, L. 2009, MNRAS, 398, 91

Raskutti, S., Greene, J. E., & Murphy, J. D. 2014, ApJ, 786, 23

Sánchez, S. F., Rosales-Ortega, F. F., Iglesias-Páramo, J., Mollá, M., Barrera-Ballesteros, J., Marino, R. A., Pérez, E., Sánchez-Blazquez, P., González Delgado, R., Cid Fernandes, R., de Lorenzo-Cáceres, A., Mendez-Abreu, J., Galbany, L., Falcon-Barroso, J., Miralles-Caballero, D., Husemann, B., García-Benito, R., Mast, D., Walcher, C. J., Gil de Paz, A., García-Lorenzo, B., Jungwiert, B., Vílchez, J. M., Jílková, L., Lyubenova, M., Cortijo-Ferrero, C., Díaz, A. I., Wisotzki, L., Márquez, I., Bland-Hawthorn, J., Ellis, S., van de Ven, G., Jahnke, K., Papaderos, P., Gomes, J. M., Mendoza, M. A., & López-Sánchez, Á. R. 2014, A&A, 563, A49

Sanderson, R. E., Garrison-Kimmel, S., Wetzel, A., Keung Chan, T., Hopkins, P. F., Kereš, D., Escala, I., Faucher-Giguère, C.-A., & Ma, X. 2017, ArXiv e-prints

Sarzi, M., Falcón-Barroso, J., Davies, R. L., Bacon, R., Bureau, M., Cappellari, M., de Zeeuw, P. T., Emsellem, E., Fathi, K., Krajnović, D., Kuntschner, H., McDermid, R. M., & Peletier, R. F. 2006, MNRAS, 366, 1151

Saulder, C., Mieske, S., Zeilinger, W. W., & Chilingarian, I. 2013, A&A, 557, A21

Walter, F., Brinks, E., de Blok, W. J. G., Bigiel, F., Kennicutt, Jr., R. C., Thornley, M. D., & Leroy, A. 2008, AJ, 136, 2563

Weijmans, A.-M., Cappellari, M., Bacon, R., de Zeeuw, P. T., Emsellem, E., Falcón-Barroso, J., Kuntschner, H., McDermid, R. M., van den Bosch, R. C. E., & van de Ven, G. 2009, MNRAS, 398, 561

Wilkinson, D. M., Maraston, C., Thomas, D., Coccato, L., Tojeiro, R., Cappellari, M., Belfiore, F., Bershady, M., Blanton, M., Bundy, K., Cales, S., Cherinka, B., Drory, N., Emsellem, E., Fu, H., Law, D., Li, C., Maiolino, R., Masters, K., Tremonti, C., Wake, D., Wang, E., Weijmans, A.-M., Xiao, T., Yan, R., Zhang, K., Bizyaev, D., Brinkmann, J., Kinemuchi, K., Malanushenko, E., Malanushenko, V., Oravetz, D., Pan, K., & Simmons, A. 2015, MNRAS, 449, 328

Willett, K. W., Lintott, C. J., Bamford, S. P., Masters, K. L., Simmons, B. D., Casteels, K. R. V., Edmondson, E. M., Fortson, L. F., Kaviraj, S., Keel, W. C., Melvin, T., Nichol, R. C., Raddick, M. J., Schawinski, K., Simpson, R. J., Skibba, R. A., Smith, A. M., & Thomas, D. 2013, MNRAS, 435, 2835

Yoachim, P., Roškar, R., & Debattista, V. P. 2010, ApJ, 716, L4
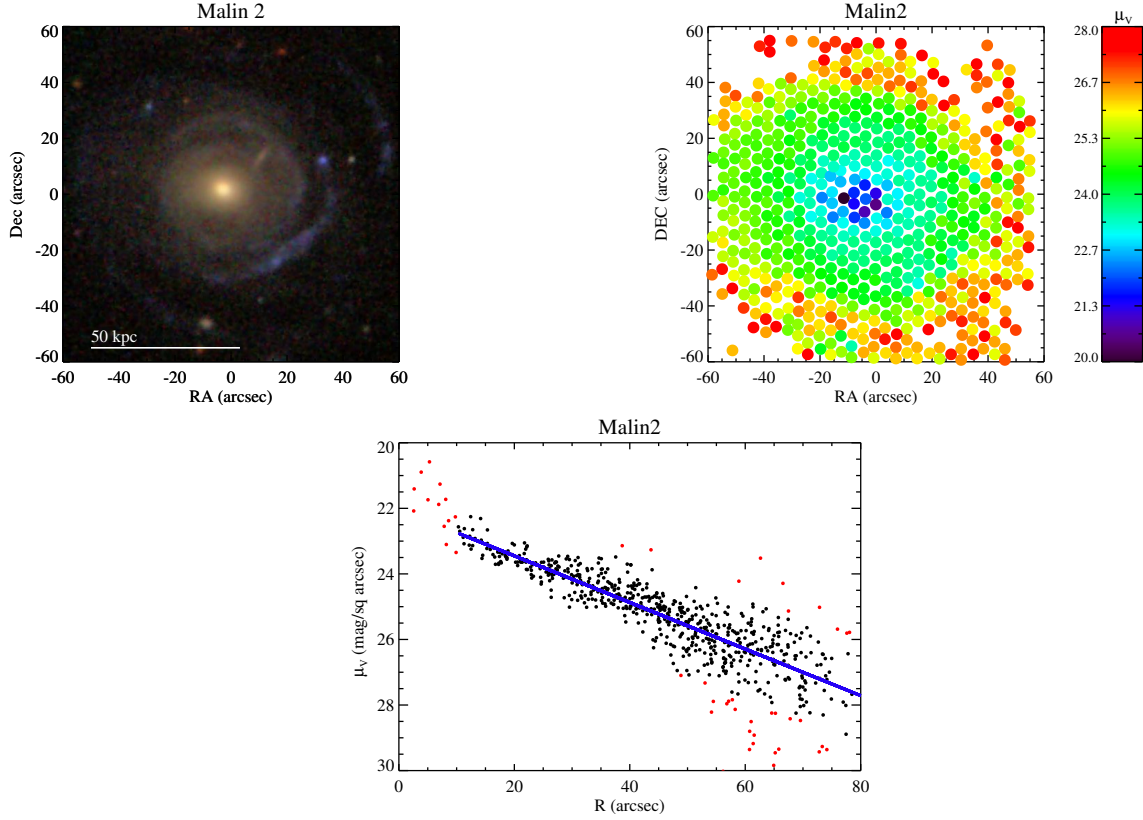
—. 2012, ApJ, 752, 97

FIG. 4.— Upper Left: SDSS image of Malin 2. Upper Right: Image made with the VIRUS-P datacube synthetic fiber magnitudes. Lower: An exponential fit to the fiber magnitudes. Red points show fibers that were clipped while the solid line shows the best-fit.
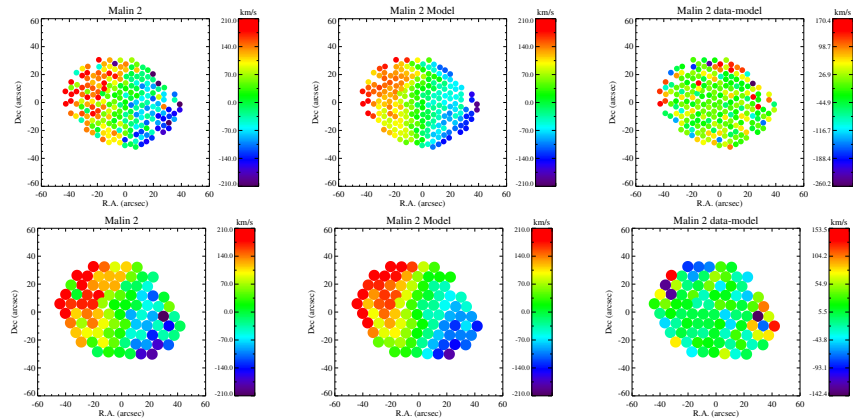

FIG. 5.— Upper panels show kinematics from individual fibers, lower panels show the results after fibers have been binned into triples. Left: Stellar velocities measured with pPXF (Cappellari & Emsellem 2004). Middle: Best fitting tilted ring model from kinemetry (Krajnović et al. 2006). Right: Best fit residuals.
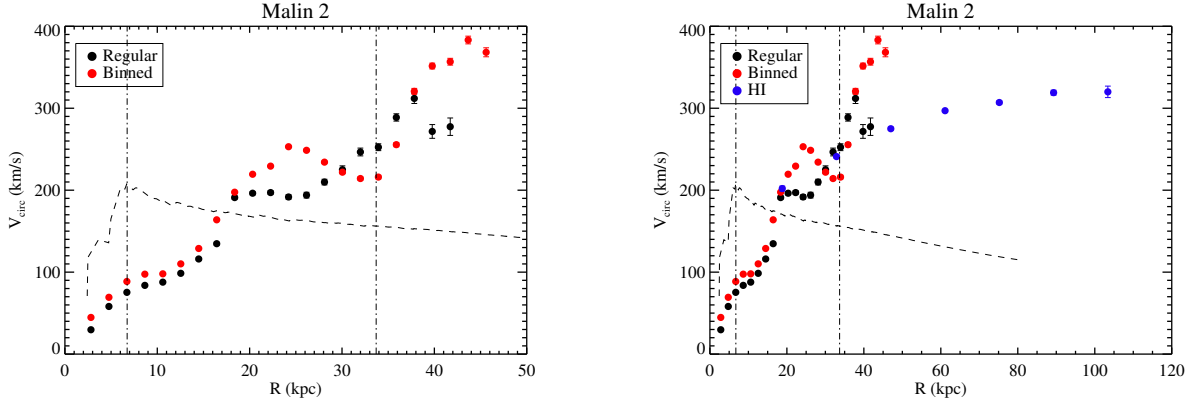
Fig. 6.— Rotation curves extracted from the best fitting models in Fig 5. The dashed curves show the expected stellar mass contribution to the rotation curve. Vertical lines mark R_e and $5R_e$. Right panel includes H I data from Pickering et al. (1997).
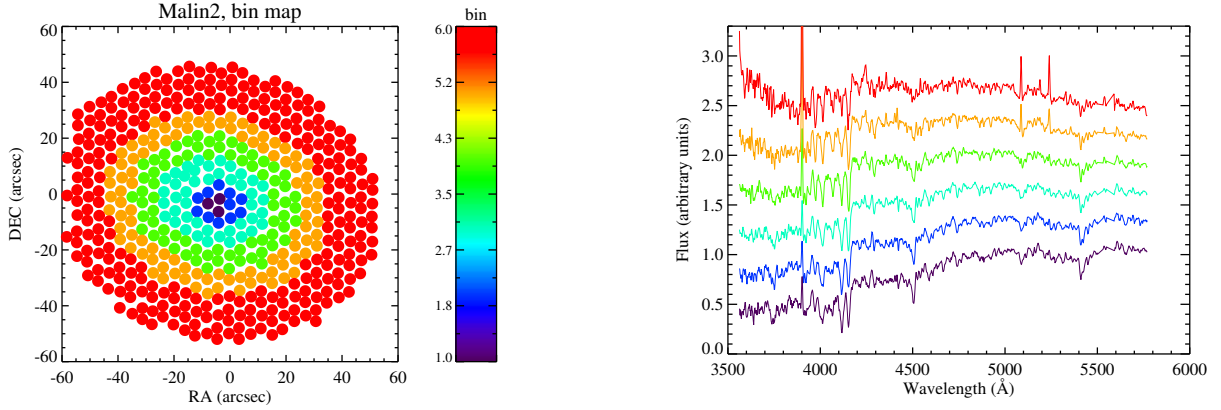
Fig. 7.— Left: Map of which fibers were binned together for star formation history measurements. Right: Resulting binned spectra, residuals from the bright skyline at 5577Å have been masked. The inner bins show strong Mg, Fe, and Ca absorption features, while the outer bins have Hβ and O III emission lines.
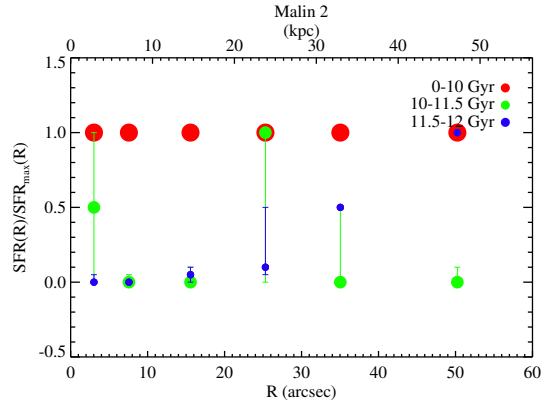
Fig. 8.— Best fitting star formation histories. For each bin, the SFH is normalized by the peak at each radius. Error bars are based on $\Delta\chi^2 = 100$ or the best fitting 4 models, whichever provides more points. The oldest age bin dominates at all radii.
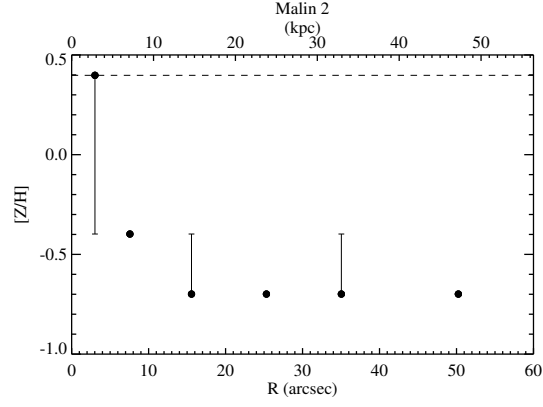
Fig. 9.— Best fitting stellar metallicities. Dashed line shows the maximum model metallicity used in the models (minimum is below the y range limit). Error bars are as in Figure 8.
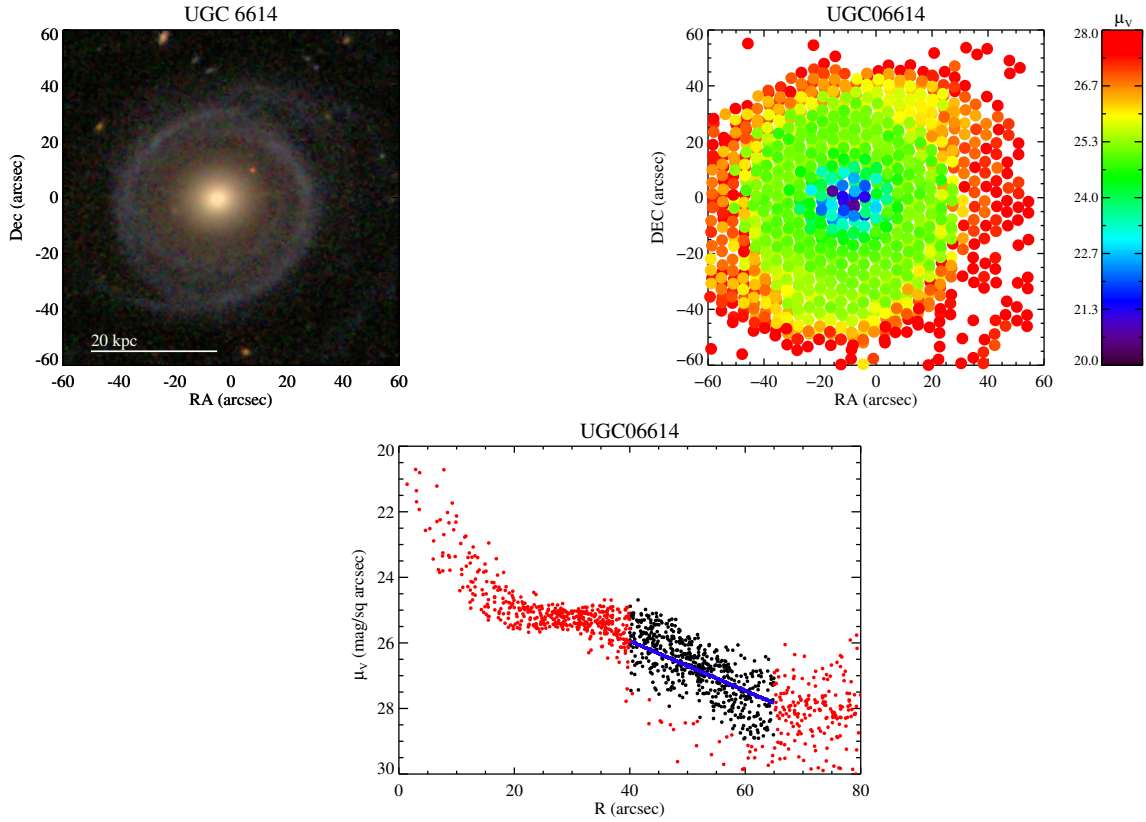

Fig. 10.— Upper Left: SDSS image of UGC 06614. Upper Right: Image made with the VIRUS-P datacube. Lower: An exponential fit to the fiber magnitudes. Red points show fibers that were clipped while the solid line shows the best-fit. We only included fibers beyond the outer ring structure.
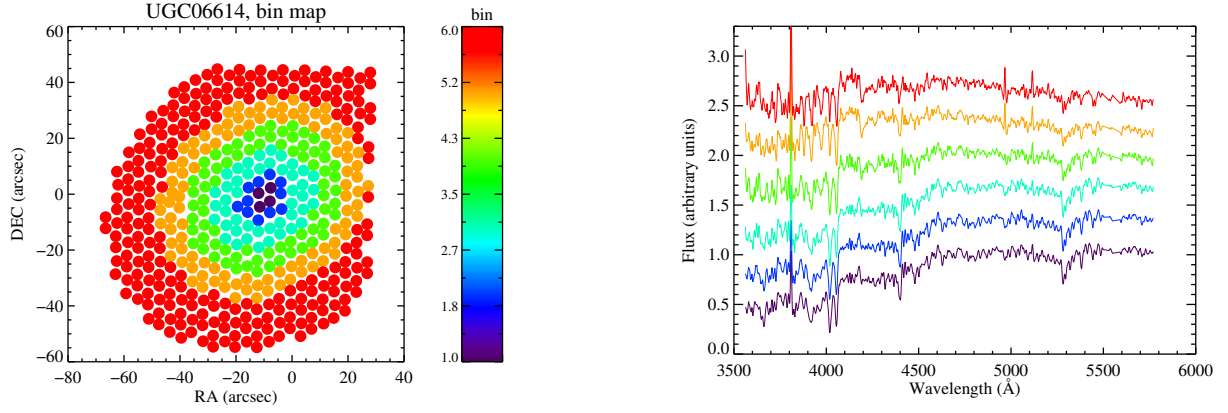
Fig. 11.— Left: Map showing which fibers were binned for UGC 6614. Right: The binned spectra, color-coded to match the map on the left. As with Malin 2, the inner spectra show strong metallicity absorption features while the outer spectra show emission lines.
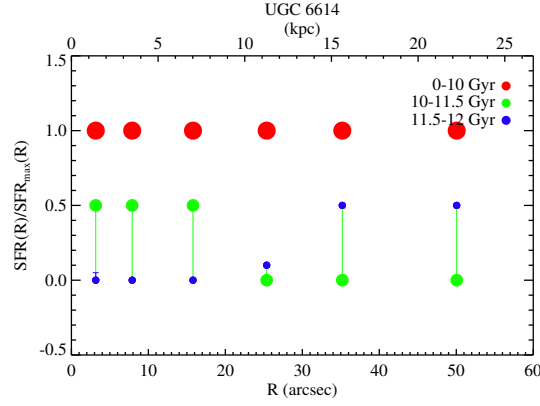

Fig. 12.— Best fitting star formation histories. For each bin, the SFH is normalized by the peak bin. Error bars are based on $\Delta\chi^2 = 100$ or the 4 best fitting models, whichever provides more points. As with Malin 2, old stars dominate at all radii.
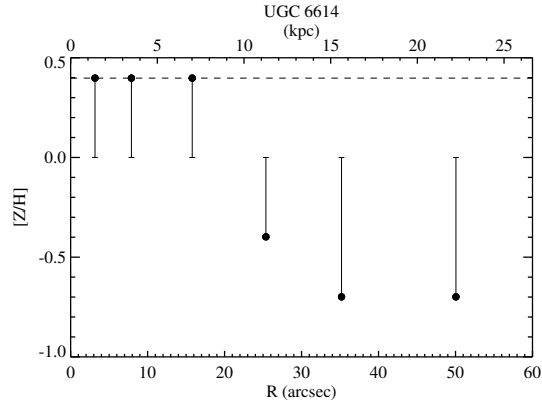

Fig. 13.— Best fitting stellar metallicities for the binned UGC 6614 spectra. Dashed line shows the maximum model value.
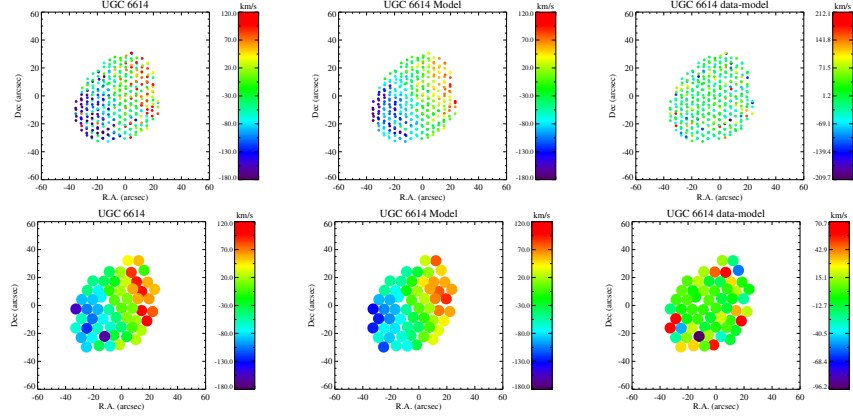
FIG. 14.— Upper panels show kinematics from individual fibers, lower panels show the results after fibers have been binned into triples. Left: Stellar velocities measured with pPXF (Cappellari & Emsellem 2004). Middle: Best fitting tilted ring model from kinemetry (Krajnović et al. 2006). Right: Best fit residuals.
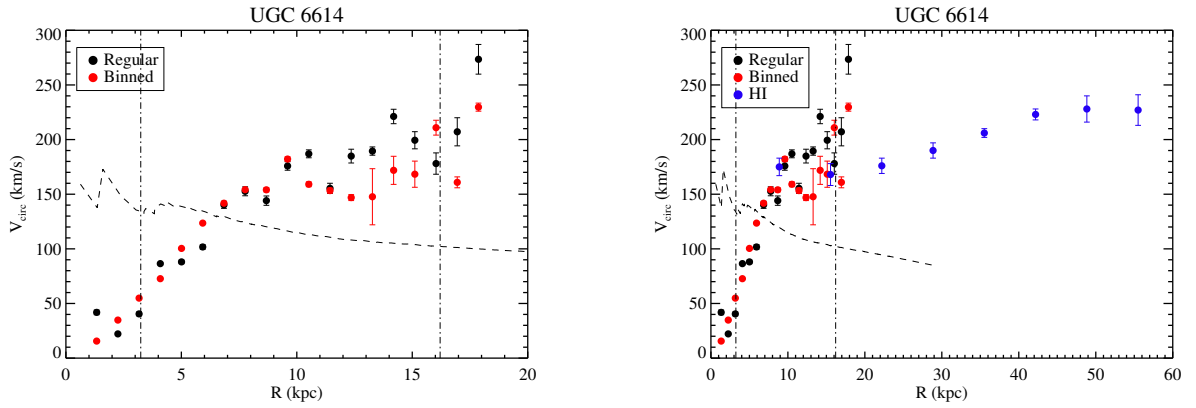

FIG. 15.— Rotation curves extracted from the best fitting model in Fig 14. The dashed curve shows the expected stellar mass contribution to the rotation curve. Vertical lines mark R_e and $5R_e$. Right panel includes H I data from Pickering et al. (1997).

APPENDIX

SDSS SQL QUERIES

To build our sample of comparison galaxies from SDSS, we used the CasJobs interface to query the SDSS DR10 database.

the galaxy CMD contours in Figure 1 were obtained via:

```
select
objid,ra,dec,
dered_u,dered_g,dered_r,dered_i,dered_z,
z,4.27E+3*z as d_hubble_mpc,
dered_u-dered_r as u_minus_r,
dered_r-5*log10(4.27E+8*z) as abs_mag_r

from specphotoall
where
class='GALAXY'
AND dered_r between 13.5 and 17.7
AND ((flags & 0x10000000) != 0)
AND ((flags & 0x8100000c00a0) = 0)
AND (((flags & 0x400000000000) = 0) or (psfmagerr_g <= 0.2))
AND (((flags & 0x100000000000) = 0) or (flags & 0x1000) = 0)
AND zerr < 0.05
AND z BETWEEN 0.01 and 0.085
AND dered_r - 5*log10(4.27E+08*z) BETWEEN -23.5 and -15.5
```

The fundamental plane contours in Figure 1 was computed from:

```
select
ph.objid, sp.z, sp.velDisp, sp.velDisperr, deVMag_g,deVMag_r, ph.deVRad_r,
ph.r,ph.dered_r, ph.extinction_r, ph.extinction_g, ph.deVAB_r,  gs.best_model_z,
gse.oh_p50, gse.lgm_tot_p50, gs.model_chisq_040, gs.model_chisq_080,
gs.model_chisq_170, gs.model_chisq_400, zoo.spiral, zoo.elliptical,
zoo.uncertain, zoo.p_el, zoo.p_cw,zoo.p_acw

from specobj as sp, photoobj as ph, galSpecIndx as gs,
galSpecExtra as gse, zoospec as zoo

where
sp.bestObjID = ph.objID and gs.specObjID = sp.specObjID
and gse.specObjID = sp.specObjID
and zoo.objid =  ph.objID

AND sp.class='GALAXY'
AND sp.velDisp != 0
AND sp.z BETWEEN 0.01 and 0.085
AND sp.zerr < 0.05
AND ph.dered_r between 13.5 and 17.7
AND ph.dered_u-ph.dered_r > 2.1
AND ph.lnLDeV_r-ph.lnLExp_r > 0.29559
AND ph.petroR90_i/ph.petroR50_i > 2.5
AND ((ph.flags & 0x10000000) != 0)
AND ((ph.flags & 0x8100000c00a0) = 0)
AND (((ph.flags & 0x400000000000) = 0) or (ph.psfmagerr_g <= 0.2))
AND (((ph.flags & 0x100000000000) = 0) or (ph.flags & 0x1000) = 0)
```

Finally, the mass-metallicity relation in Figure 1 was obtained via:

```
select
ph.objid,sp.velDisp, gse.lgm_tot_p50, gs.lick_hd_a_sub, gs.lick_hd_f_sub,
gs.lick_cn1_sub, gs.lick_cn2_sub, gs.lick_Ca4227_sub, gs.lick_G4300_sub,
gs.lick_hg_a_sub, gs.lick_hg_f_sub, gs.lick_fe4383_sub, gs.lick_ca4455_sub,
gs.lick_fe4531_sub, gs.lick_c4668_sub, gs.lick_hb_sub, gs.lick_fe5015_sub,
gs.lick_mg1_sub, gs.lick_mg2_sub, gs.lick_mgb_sub, gs.lick_Fe5270_sub,
```

```
gs.lick_Fe5335_sub, gs.lick_Fe5406_sub, gs.lick_Fe5709_sub, gs.lick_Fe5782_sub,
gs.lick_NaD_sub, gs.lick_TiO1_sub, gs.lick_TiO2_sub

from specobj as sp, photoobj as ph, galSpecIndx as gs, galSpecExtra as gse

where
sp.bestObjID = ph.objID and gs.specObjID = sp.specObjID
and gse.specObjID = sp.specObjID
AND sp.class='GALAXY'
AND sp.velDisp != 0
AND sp.z BETWEEN 0.01 and 0.085
AND sp.zerr < 0.05
AND ph.dered_r between 13.5 and 17.7
AND ph.dered_u-ph.dered_r > 2.1
AND ph.lnLDeV_r-ph.lnLExp_r > 0.29559
AND ph.petroR90_i/ph.petroR50_i > 2.5
AND ((ph.flags & 0x10000000) != 0)
AND ((ph.flags & 0x8100000c00a0) = 0)
AND (((ph.flags & 0x400000000000) = 0) or (ph.psfmagerr_g <= 0.2))
AND (((ph.flags & 0x100000000000) = 0) or (ph.flags & 0x1000) = 0)
```